Replicating the rolling-sliding dynamics of cam-roller contacts in large-scale hydraulic drivetrains

A small-scale approach

Amoroso, Pedro; van Ostayen, Ron A.J.; de Rooij, Matthijn B.

DOI
10.1177/13506501241242185

Publication date
2024

Document Version
Accepted author manuscript

Published in
Proceedings of the Institution of Mechanical Engineers, Part J: Journal of Engineering Tribology

Proc IMechE Part J: J Engineering Tribology
XX(X):1–17

DOI: 10.1177/ToBeAssigned
www.sagepub.com/
SAGE

Replicating the Rolling-Sliding Dynamics of Cam-Roller Contacts in Large-Scale Hydraulic Drivetrains: A Small-Scale Approach

Pedro Amoroso[1,2], Ron A.J. van Ostayen [1] and Matthijn B de Rooij[2]

Abstract

The rolling-sliding dynamics of large-scale cam-roller contacts are strongly influenced by the inertia of the roller, particularly when slippage occurs. Slippage can potentially impact the reliability of these rolling interfaces. This study introduces an approach to replicate the rolling-sliding dynamics of cam-roller contacts in a large-scale hydraulic drivetrain, on a small scale. For that, we have upgraded our two-roller tribometer to enable cyclic loading, allow the application of resisting torques, and generate inertia torques. These are three essential elements required to mimic the dynamics observed at large scales. A method has been proposed for scaling the roller inertia accordingly. Furthermore, we have implemented a modeling framework from previous work to make predictions under various dynamic conditions. The results show that our small-scale approach can replicate five key characteristics anticipated at a large scale, including those linked to slippage. Small increments in the resisting torque significantly increased the slide-to-roll ratio (SRR) and peak traction force, among others. The simulations also predicted these effects, capturing trends and producing reasonable predictions of the magnitude and relevant features of key parameters. The use of cyclic loading, extra inertia, and adjustable resisting torques, effectively generated repeatable and controllable dynamic rolling-sliding conditions. Our work is significant for the design and development of novel large-scale hydraulic drivetrains. Our findings highlight the importance of reducing slippage at low contact forces to prevent the brusque change in the rolling conditions during the high contact force phase. By doing so, surface damage and detrimental dynamic effects can be prevented.

Keywords

tribological testing, rolling-sliding, cam-roller, hydraulic drivetrain, roller slippage

Introduction

The development of highly efficient, reliable, and low-maintenance systems for power generation plays a crucial role in the transition to cleaner and renewable energy production. Such attributes have been acknowledged in fluid power technology due to its robustness, reliability, and simplicity. Recognizing these advantages, several companies have gradually incorporated hydraulic technology in different systems for wind energy generation[1]. For example, one of the promising ideas is the replacement of overly complex transmissions and electronics of offshore wind turbines with a novel large-scale hydraulic drivetrain (HD). This large-scale HD is in essence a multi-MW radial piston pump with seawater as the hydraulic fluid[2,3] (Figure 1).

In a large-scale HD, cam-roller follower mechanisms are utilized to efficiently transform rotary motion into linear motion and carry out the pumping function. The contact between the cam and the roller within the HD is a critical interface bearing the loads generated by millions of pumping cycles over the HD's lifespan[4,5]. At this interface, optimum lubrication must be ensured for a smooth, reliable, and long-lasting operation. Figure 2 shows the forces acting at this contact. The total force F_T generated during pumping results in a contact force F_c. The traction force at the cam-roller interface F_t generates a tractive torque τ_t. This tractive torque is proportional to the sum of the frictional torque τ_f produced by the internal spherical roller bearings and the inertia torque τ_i generated during accelerations. The reaction force R_x results from the side force counteracted by a linear guiding system[5] (Figure 1).

Previous research on the rolling-sliding dynamics of cam-roller contacts is mostly focused on smaller scales. A few decades ago, Gecim[6] acknowledged the possibility of roller slippage and predicted the traction force required for no-slip conditions at the cam-roller contact in a valvetrain system. The author concluded that the inertia torque plays an important role, particularly at high speeds[6]. Duffy[7] showed experimentally that slippage occurs in a predictable pattern and concluded that the inertia of the roller limits its angular

[1] Department of Precision and Microsystems Engineering, Delft University of Technology, Mekelweg 2, 2628 CD Delft, The Netherlands
[2]Faculty of Engineering Technology, University of Twente, Enschede, The Netherlands

Corresponding author:
Pedro Amoroso, Department of Precision and Microsystems Engineering, Delft University of Technology, Mekelweg 2, 2628 CD Delft, The Netherlands
Email: P.AmorosoFeijoo@tudelft.nl

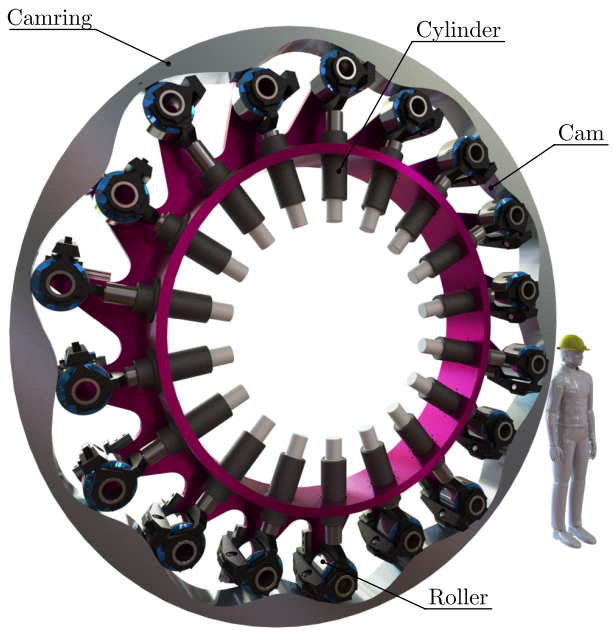

Figure 1. Cross-section of a large-scale Hydraulic Drivetrain (HD) with cam-roller followers.

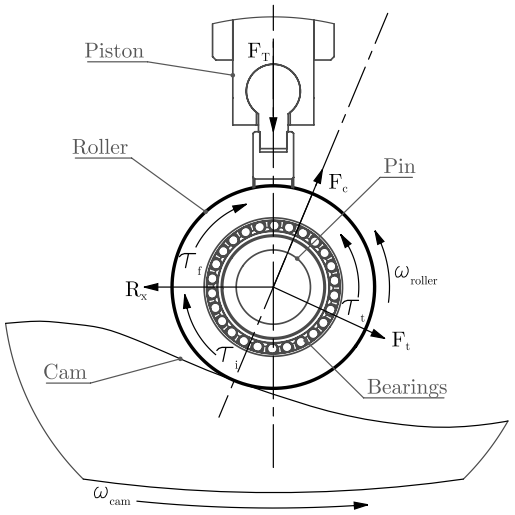

Figure 2. Forces acting at the cam-roller contact.

acceleration. As a consequence, slippage occurs during rapid changes in the surface velocity of the cam. Lee et al[8,9], pointed out that wear remains an issue in cam-roller contacts of valvetrain systems if slippage occurs. The authors showed that at higher engine speeds (750-1500 rpm), the torque of inertia is in the same order of magnitude as the frictional torque generated by the journal bearing inside the roller follower[8,9]. Ji et al[10], developed a lubrication model to estimate the level of slippage in a cam-roller contact of a valvetrain. Likewise, the authors concluded that slippage is likely to take place on the flanks of the cam, where high accelerations occur, as the inertia of the roller plays an important role[10]. Alakhramsing et al[11,12], studied the tribology of cam-roller contacts in diesel injection systems, accounting for the effects of the roller inertia and frictional torque. Similarly, the authors concluded that inertia becomes relevant only at high rotational speeds[11,12]. As stated earlier, these studies are centered on small scales, for example, the diameter of the roller follower in reference[6] is 17.8 mm, and 36 mm in references[11,12]. The latter diameters are approximately 16.8 and 8.3 times smaller, respectively than the diameter of a roller follower in a large-scale hydraulic drivetrain[5]. Furthermore, the inertia of these rollers is thousands of times smaller than that of a roller follower in a large-scale HD.

In recent work, the rolling-sliding dynamics of cam-roller contacts in a large-scale HD were examined[5]. The theoretical study predicts that roller slippage occurs due to the interplay of forces and torques described earlier (Figure 2). The results show that the inertia of the roller contributes to slippage to a large extent, as it limits its angular acceleration. Furthermore, this large inertia causes dynamic effects which are amplified, particularly when slippage occurs. In fact, the occurrence of slippage under low contact forces leads to interesting dynamics caused by abrupt changes in the rolling condition at the beginning of the high contact force phase. High traction force peaks arise due to the brusque change from rolling-sliding to virtually pure rolling. Such behavior displays a striking similarity to that of rollers in large, slow-moving bearings carrying radial unidirectional loads. In these components, the rollers are prone to slip (i.e., slide) at the unloaded region and rapidly accelerate upon entering the high-load region[13,14]. Under these conditions, smearing damage is likely to occur[14,15].

Tribological testing is vital in achieving high reliability and efficiency in large-scale hydraulic drivetrains (HDs). From an experimental point of view, a close replication of the conditions experienced by the cam-roller contact is highly desirable. Moreover, from a model validation perspective, the idea of a simplified dynamic tribological test with good control over different variables is very attractive. However, as far as our knowledge extends, there has been no such development. Most of the previous research is focused on cam-roller follower contacts in valvetrain[6–10,16–19] and diesel injection systems[11,12,20] at much smaller scales.

Considering tribological testing aspects, conventional two-disc tests with fixed SRR and stable loading conditions, have limited representativeness with respect to the real-life dynamics. On the other hand, experiments at the component level (with actual cams) can generate such dynamics, but they suffer from reduced practicality and control over variables.

To address the above-mentioned challenges, we have developed an original small-scale experimental approach in an attempt to replicate the rolling-sliding dynamics of cam-roller contacts in large-scale HDs. This approach is innovative as it can be employed to represent a tribological system in terms of dynamic effects induced by inertia apart from other commonly selected parameters such as contact pressure, materials, motion, and lubrication regime. For that, we have used a two-roller tribometer[21] developed in-house that enables cyclic loading, allows the application of resisting torques, and generates inertia torques. In addition, we have introduced a novel approach to scale the inertia of the large-scale roller accordingly. In that way, dynamic effects have become noticeable at a small scale. We have confirmed the validity of this approach using experimental

results. Furthermore, to support our experimental work, the theoretical framework presented in previous work[5] has been implemented to predict the rolling-sliding performance of the test rollers under various dynamic conditions. In this way, the model's effectiveness in capturing the rolling-sliding dynamics can be assessed.

Our study aims to enhance the representativeness of small-scale tribological tests conducted during the design and development phase of novel large-scale HDs. Ultimately, this will enable a more comprehensive understanding of the rolling-sliding dynamics of roller followers in hydraulic drivetrains from a tribological point of view.

Rolling-Sliding Dynamics

In this study, we present an attempt to replicate the rolling-sliding dynamics of a large-scale tribosystem (i.e., the cam-roller contact in a large-scale HD) on a smaller scale (i.e., the roller-on-roller contact in a tribometer). To distinguish the large-scale system from the small-scale system, the superscripts input (^{i}) and output (^{o}) are employed consistently throughout this work. This notation allows for a clear distinction between the original system to be scaled (input) and the resultant system on a small scale (output).

To start, it is essential to provide a concise overview of the rolling-sliding dynamics involved in the input system, i.e., the cam-roller contacts within a large-scale HD. Based on prior research[5], Figure 3 contains 6 graphs showing the variation of different parameters during one pumping cycle. One pumping cycle lasts approximately $0.4\,\mathrm{s}$ and comprises the compression phase, (where the contact force F_c^i steeply increases) and the suction phase, (where the contact force F_c^i rapidly drops).

Figure 3a shows the slide-to-roll ratio (SRR^i), the normalized contact force $F_c^i/F_{c_{max}}^i$, and the normalized displacement profile (σ/σ_{max}). The SRR^i is equal to $(u_c+u_r)/u_m$, where u_c and u_r are the cam and roller surface velocities and u_m is the lubricant's mean entrainment velocity, respectively. In the SRR^i profile, four key characteristics are highlighted: (1) the roller slips at low contact forces, (2) the roller enters the high contact force phase with a certain level of slippage, (3) the roller transitions rapidly from rolling-sliding to virtually pure rolling, (4) the roller rolls without slipping under high contact forces, and then, the cycle repeats. A fifth characteristic (5), the large peak in the traction force F_t^i, is highlighted in Figure 3b. This traction force peak occurs as a result of the rapid change in the rolling conditions described above. Likewise, the latter is also responsible for the peak in the roller's angular acceleration $\dot{\omega}^i$ shown in Figure 3c.

As mentioned earlier, the behavior described above exhibits a strong similarity to that of rollers in large, slow-moving bearings carrying radial unidirectional loads (e.g., the main bearings of large-scale wind turbines). Evans et al.[14] developed a tribological testing protocol for generating smearing on actual cylindrical roller bearings. The authors proposed the "smearing criterion" $\phi = \mu P_{max} u_s$ to identify the onset of smearing, where μ is the traction coefficient at the rolling interface, P_{max} is the maximum Hertzian contact pressure, and u_s is the sliding velocity. Figure 3d shows the smearing criterion ϕ^i derived from previous work[5]. In this graph, it is interesting to see that a peak in the smearing criterion profile is generated due to the occurrence of slippage in combination with high contact pressures. This provides valuable information regarding the location and intensity of the frictional power, and hence, it is useful for identifying cam regions where smearing damage is more likely to occur.

Finally, Figures 3e and 3f show the Hertzian contact area A^i and the shear stress τ^i acting over this area, respectively. These plots will come in handy in the following sections to further describe and validate our approach.

Test Setup

To replicate the dynamics mentioned earlier using a two-roller tribometer, three crucial elements are necessary: rapid load variations, extra inertia, and the ability to generate and regulate slippage at low loads. To achieve that, we have upgraded our two-roller tribometer developed in-house, the "Cam-Roller interface Tribotester (CRT)"[21]. A thorough description of this test setup can be found in reference[21].

Figure 4 shows the internal components of the CRT. The test setup consists of (1) a driving system that rotates the bottom roller (R1) at stable speeds, (2) a braking system that applies precise and stable braking torques on the top roller (R2), and (3) a loading system which can generate cyclic contact forces between the rollers. This is achieved by using an air bellow and a proportional pressure regulator with a fast dynamic response.

In Figure 4, the the motor (4) drives R1 (5) and R1 drives R2 (6) thanks to the traction generated at the interface. The traction force is measured by a compression load cell located in line with the center of R1, without the introduction of parasitic friction forces[21]. The test rollers R1 and R2 have a $54\,\mathrm{mm}$ diameter. R1 has a flat length of $34\,\mathrm{mm}$, whereas R2 has a step with a flat length of $11\,\mathrm{mm}$ and crowned edges. The rollers R1 and R2 are used to represent the cam and the roller follower, respectively. Both rollers are mounted on keyless locking devices to fix them on their shafts. The shafts are supported by two needle bearings (7a and 7b), that allow them to rotate with minimum resistance under heavy loads. The shaft of R2 is coupled to a magnetic hysteresis brake (8) with an inbuilt flywheel (9). The brake is used to apply precise resisting torques on R2 and the flywheel adds extra inertia to R2. Further details on the reason for adding inertia will be given below. The torque sensor (10) located in line with the shaft of R2 measures the applied braking torques and the inertia torques.

It is important to note that the torque sensor only captures the applied braking torque and the inertia torque generated by the inertia located on its right side (with respect to the centerline in Figure 4). Hence, the frictional torque produced by the needle bearings is not accounted for in the torque sensor measurements. This possibility becomes useful to isolate the effects produced by different torques. Finally, the rotational speed of R2 and R1 is measured by the encoders 11a and 11b, respectively.

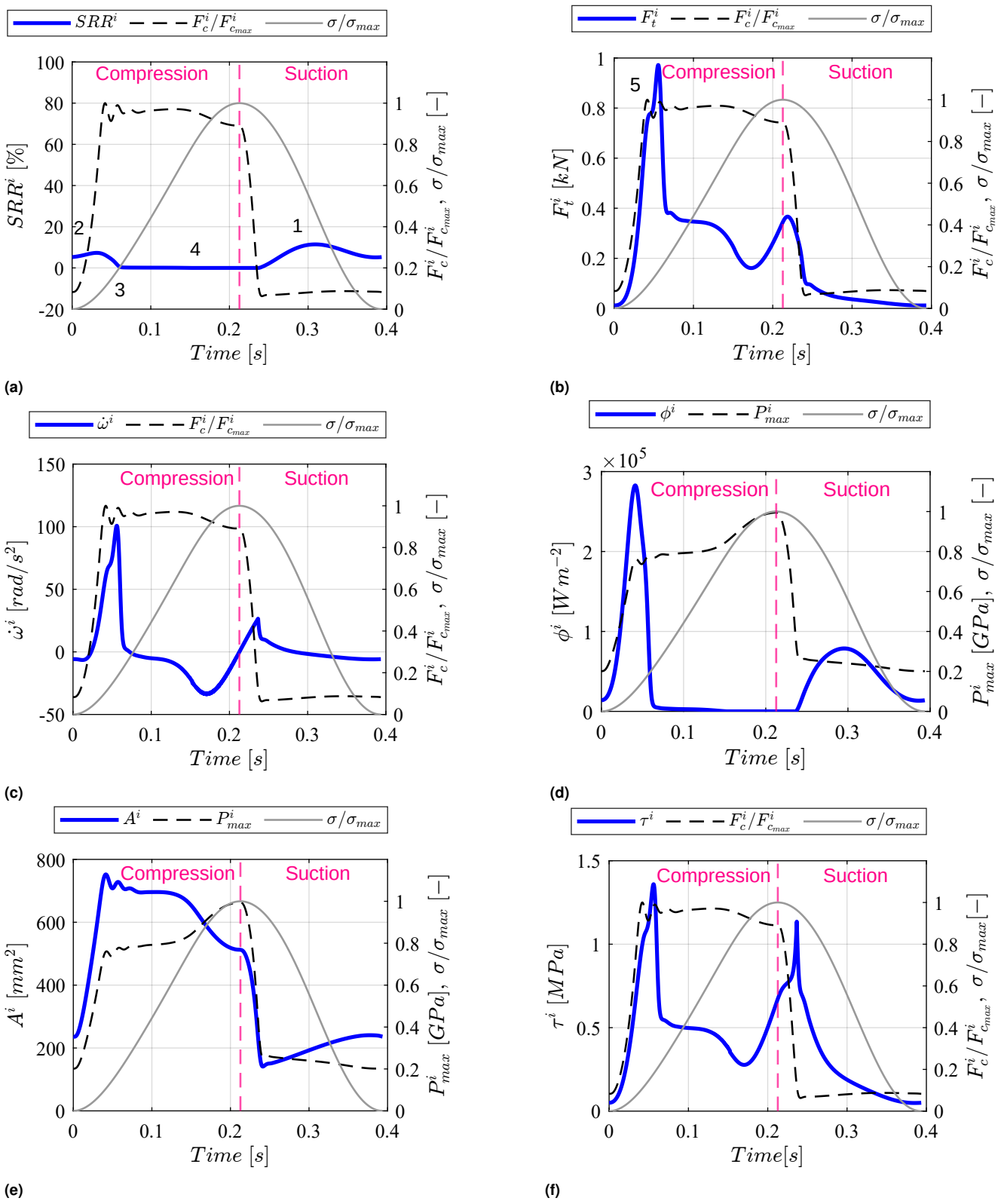

Figure 3. Rolling-sliding dynamics of the cam-roller contacts in a large-scale HD[5].

Scaling Factors

As mentioned earlier, the effects of inertia in cam-roller contacts become much more significant at larger scales. For that reason, we have centered our effort on replicating such effects on a smaller scale and with a simplified rolling pair configuration. To achieve that, we have used a set of factors to downscale the input system as explained below.

Geometrical Scaling Factors

A set of factors has been selected for downscaling the size of the input roller. These factors have been defined considering both, the geometrical constraints in the test setup and the reference conditions in the input system as described next.

The dimensions of the input roller, including the outer radius $r_o^i = 0.150\,\mathrm{m}$, inner radius $r_i^i = 0.1125\,\mathrm{m}$, and length

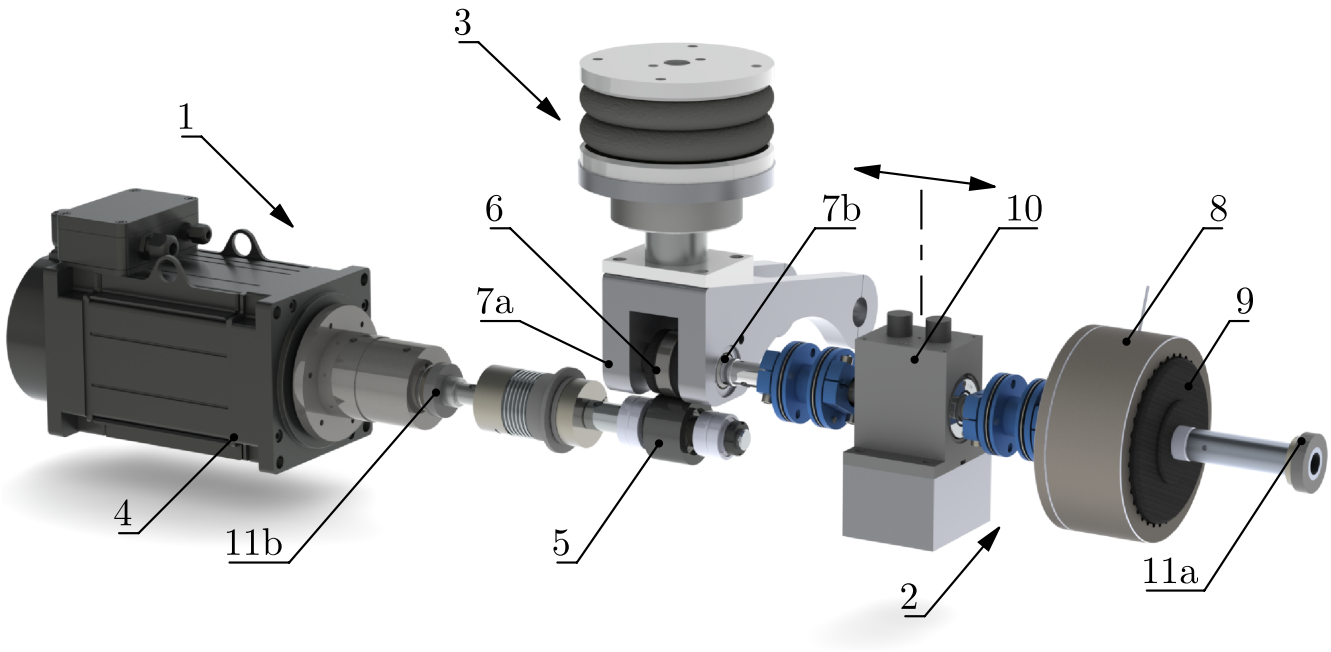

Figure 4. Cam-Roller interface Tribotester (CRT). Driving system (1), braking system (2), loading system (3), motor (4), (R1) bottom roller (5), (R2) top roller (6), needle bearings (7a and 7b), magnetic hysteresis brake (8), inbuilt flywheel (9), torque sensor (10), and encoders (11a and 11b).

$l_r^i = 0.165\,\mathrm{m}$, can be transformed into the dimensions of the output roller by dividing them by the factors $S_1 = 5.55$, $S_2 = 5.92$, and $S_3 = 5.5$, respectively. The resulting dimensions for R2 are: outer radius $r_o^o = 0.027\,\mathrm{m}$, inner radius $r_i^o = 0.019\,\mathrm{m}$, and length $l_r^o = 0.03\,\mathrm{m}$. The outer radius of the bottom roller (R1) is the same as that of the top roller (R2). Additionally, the input contact length $B^i = 150\,\mathrm{mm}$ can be transformed into the output contact length $B^o = 11\,\mathrm{mm}$ by using the scaling factor $S_4 = 13.63$. The latter factor has been selected to ensure that the minimum and maximum contact pressure P_{max}^i (Figure 3) in the input system (i.e., 0.2 and 1 GPa, respectively) can be generated in the output system with the given load range (i.e., 0.2 to 4 kN). The outer and inner radius of the bottom roller (R1) are the same as that of the top roller (R2).

Inertia in the Input and Output Systems

In the output system (i.e., the test setup), the top roller (R2) represents the roller follower of the input system (i.e., the large-scale HD). Having defined the geometry of R2, the inertia of the output roller can be compared to that of the input roller. The output roller inertia is given by $0.5\pi l_r^o \rho_{R2}^o[(r_o^o)^4 - (r_i^o)^4]$, where ρ_{R2}^o the density of the output roller. Assuming that $\rho_{R2}^o = 7800\,\mathrm{kg\,m^{-3}}$ the output roller inertia I_r^o is $1.47 \times 10^{-4}\,\mathrm{kg\,m^2}$. On the other hand, the total roller inertia in the input system considered for this study is $I_r^o = 0.90\,\mathrm{kg\,m^2}$. This value accounts not only for the roller inertia but also the inertia of extra components rotating with it (e.g., internal bearings and thrust covers).

Here, it is crucial to highlight that despite the output roller dimensions being roughly 5.5 times smaller than the input roller, the inertia of the output roller is ≈ 6122 times smaller. Therefore, if the roller inertia (I_r^o) in the output system is maintained, the effects of inertia would be negligible under dynamic testing conditions. For that reason, an approach is required to downscale the input roller inertia accordingly.

Approach for Scaling Inertia

To address the challenge described above, we propose an approach to downscale the inertia of the input roller (I_r^i) in order to account for significant dynamic effects. As a result, the rolling-sliding dynamics observed at large scales (Figure 3) could be replicated on a smaller scale.

In the input system, neglecting the frictional torque, the traction force F_t^i required to reach a peak acceleration $\dot{\omega}^i$ with a roller inertia I_r^i is given by:

$$F_t^i = \frac{\dot{\omega}^i I_r^i}{r_o^i} \tag{1}$$

Assuming that the contact between the cam and the roller forms a rectangular Hertzian contact area, A^i, the shear stress τ^i produced by the traction force F_t^i over this area can be computed as:

$$\tau^i = \frac{\dot{\omega}^i I_r^i}{A^i r_o^i} \tag{2}$$

where A^i represents the contact area resulting from the contact pressure generated at the moment when the peak acceleration $\dot{\omega}^i$ is reached. This area is given by:

$$A^i = 2b^i B^i \tag{3}$$

where $2b^i$ is the Herzian contact width and B^i is the contact length.

The followed approach for downscaling the input system inertia I_r^i relies on balancing the shear stress for the input and output systems (i.e., $\tau^i = \tau^o$) and two assumptions: (1) A peak acceleration $\dot{\omega}$ can be generated in both, the input

and output systems, and (2) the maximum contact pressure P_{max} at the time the peak acceleration occurs is the same for both, the input and output systems. The validity of these assumptions will be discussed later on in section "Results and Discussion".

After equating the shear stresses, and assuming that $\dot{\omega}^i = \dot{\omega}^o$, the following expression can be obtained:

$$\frac{I_r^i}{I_r^o} = \frac{A^i r_o^i}{A^o r_o^o} \tag{4}$$

Substituting r_o^i/r_o^o with the respective scaling factor S_1, the expression above is reduced to:

$$\frac{I_r^i}{I_r^o} = S_1 \frac{A^i}{A^o} \tag{5}$$

In Eq.5, $S_1 \frac{A^i}{A^o}$ is equal to the scaling factor S_5, which is used to downscale the input inertia I_r^i.

In eq.3, the contact witdth b^i can be substituted by:

$$b^i = \frac{2F_c^i}{\pi B^i P_{max}^i} \tag{6}$$

A similar substitution can be made for b^o, resulting in the creation of two new expressions for A^i and A^o. By substituting these new expressions in eq.5, a new expression to calculate S_5 can be obtained. Since $P_{max}^i = P_{max}^o$, based on the second assumption above, the expression can be reduced to eq.7. In eq.7, F_c^i and F_c^o are the contact forces that generate a determined maximum Hertzian contact pressure P_{max} in both, the input and output systems, at the point where the peak acceleration occurs.

$$S_5 = \frac{I_r^i}{I_r^o} = S_1 \frac{F_c^i}{F_c^o} \tag{7}$$

It is important to highlight that by following the approach proposed above, I_r^o should be substantially increased in relation to its original value ($1.47 \times 10^{-4}\,\mathrm{kg\,m^2}$). This justifies the use of a brake with an inbuilt flywheel (Figure 4) coupled to the top roller shaft. The approach presented above will be used in section "Materials and Methods" to provide the scaling factor S_5 and the new value for I_r^o.

Estimation of Traction and Roller Slippage

Providing a reasonable estimation of the expected behavior during the experiments is very valuable to support our experimental work. For this purpose, we have implemented the approach presented in reference[5] to predict the rolling-sliding dynamics of the test rollers under cyclic loading conditions in the output system. In that way, theoretical and experimental results can be compared to assess the ability of the model to capture the rolling-sliding dynamics of the contact. For a complete description of the modeling framework adopted in this work, the interested reader is referred to reference[5].

Torque balancing

Figure 5 shows a schematic of the forces and torques acting on the rollers of the test setup (Figure 4). A load is applied to generate a contact force F_c^o between R1 and R2. R1 is driven

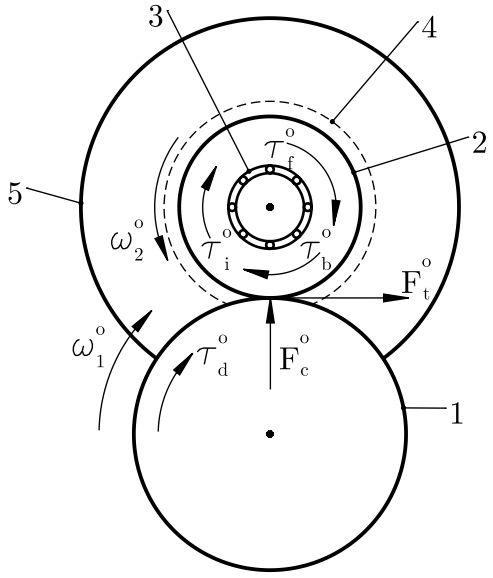

Figure 5. Forces and torques acting on the test rollers. (R1) bottom roller (1), (R2) top roller (2), needle-bearing arrangement (3), inbuilt flywheel (4), magnetic hysteresis brake (5).

by a torque τ_d^o at a stable speed ω_1^o. R2 rotates at a speed ω_2^o, which strongly depends on the traction force F_t^o generated at the interface. The needle bearings (3), the flywheel (4) and the magnetic hysteresis brake (5) generate the resisting torques τ_f^o, τ_i^o and τ_b^o, respectively, which act on R2. The traction force F_t^o developed at the interface, is proportional to the sum of these torques as shown in the equations below.

Eq. 8 represents the torque balance[5,12], which governs the velocity of R2, where τ_t^o is the tractive torque, τ_f^o the total frictional torque, τ_b^o the braking torque, and τ_i^o the inertia torque. This equation couples two tribological systems: one constituted by the contact between the test rollers and the other by the needle bearings. Consequently, the frictional torque generated by the needle bearings exerts an influence on both the traction force F_t^o and the the SRR^o occurring at the contact between R1 and R2. Likewise, the frictional torque produced within the needle bearings is dependent on the angular velocity ω_2. This equation can be solved iteratively as discussed in prior studies[5,11,12,20].

$$\tau_t^o = \tau_f^o + \tau_b^o + \tau_i^o \tag{8}$$

The tractive torque τ_t^o is equal to $F_c^o \mu^o r_o^o$, where μ^o is the traction coefficient, and thus, $F_c^o \mu^o = F_t^o$. The total frictional torque τ_f^o is the sum of the frictional torques produced by the needle bearings 7a ($\tau_{f_{7a}}^o$) and 7b ($\tau_{f_{7b}}^o$). The inertia torque τ_i^o is equal to $I_r^o \dot{\omega}_2^o$, where I_r^o is the scaled roller inertia and $\dot{\omega}_2^o$ is the angular acceleration of R2. Eq. 9 can be obtained by substituting the expressions above in eq. 8.

$$F_c^o \mu^o r_o^o = \tau_{f_{7a}}^o + \tau_{f_{7b}}^o + \tau_b + I_r^o \dot{\omega}_2^o \tag{9}$$

Estimation of the Traction Coefficient

In eq.9, the traction coefficient μ^o is strongly dependent on the sliding velocity $u_s^o = |u_1^o - u_2^o|$, and it can be estimated

by using the expression provided by Masjedi & Khonsari[22]. For a more in-depth understanding of this approach for estimating traction, the interested reader is referred to reference[22], which provides comprehensive details.

The lambda ratio $\lambda = h_{min}/\sigma^*$ has been employed to determine the lubrication regime, where h_{min} is the minimum film thickness (calculated with the expressions in reference[22]) and σ^* is the composite surface roughness. Since we have conducted the experiments at high lambda ratios, ensuring that there is no asperity contact, the traction formula in reference[22] can be reduced to:

$$\mu^o = \frac{F_t^o}{F_c^o} = \frac{2b^o B^o \tau_{\text{lim}}^o}{F_c^o}\left[1 - \exp\frac{-\eta_{\text{avg}\circ} u_s^o}{\tau_{\text{lim}}^o\, h_c^o}\right] \tag{10}$$

where τ_{lim}^o is the limiting shear stress, η_{avg}^o the average viscosity (computed as per the Roeland's equation in reference[22]), and h_c^o the central film thickness. The central film thickness h_c^o has been computed by using the formula proposed by Moes[23], as it covers are wide range of operating conditions in concentrated line contacts[23,24].

Estimation of the Frictional Torque

Chiu & Myers[19] derived an empirical expression to estimate the frictional torque in needle bearings that accounts for the viscous and load-dependent bearing torque and neglects seal friction. This expression (eq. 11) has been implemented in this work to estimate the frictional torque produced by the needle bearings in the test setup (Figure 4). It should be noted that the needle bearings 7a and 7b have an open (i.e., unshielded) design, and hence, there is no need to account for seal friction.

In eq.9, the frictional torque generated by the needle bearing 7a ($\tau_{f_{7a}}^o$) can be estimated by using eq.11, where, ν is the kinematic viscosity of the lubricant, and n is the bearing speed (in rpm). Likewise, the frictional torque generated by the needle bearing 7b ($\tau_{f_{7b}}^o$) can be computed with eq.11 by replacing $d_{m_{7a}}$ with the corresponding mean bearing diameter $d_{m_{7b}}$. It should be noted that the force F_t^o acting on the needle bearings (Figure 5) has been neglected, as it is very small and does not cause any significant change in the estimated frictional torque.

$$\tau_{f_{7a}}^o = 4.5 \cdot 10^{-10} \nu^{0.3} d_{m_{7a}} n^{0.6} + 1.2^{-4} d_{m_{7a}} (0.5 F_c^o)^{0.41} \tag{11}$$

Torque, Speed, and Force Measurements

The sensor configuration in the CRT (Figure 4) can be used to our advantage, allowing us to isolate different resisting torques. For example, as explained above, the torque measured by the torque sensor (τ_m^o) comprises the applied braking torque τ_b and part of the inertia torque τ_i. The inertia acting "after" the torque sensor (i.e., on the right side) is defined as I_a, and the inertia acting "before" (i.e., on the left side) is defined as I_b. Thus, the torque of inertia measured by the torque sensor is $I_a^o \dot{\omega}_2^o$, where $\dot{\omega}_2^o$ can be computed by deriving the measured angular velocity ω_2^o with respect to time. Furthermore, the measured traction force F_t^o can be used to calculate the tractive torque τ_t, which is equal to $\tau_f^o + \tau_b^o + \tau_i^o$. As a result, the following equations can be obtained to calculate all the torques in eq. 8, based on the torque (τ_m^o), traction force (F_t^o), and angular speed (ω_2^o) measurements.

$$\tau_t^o = F_t^o r_o^o \tag{12}$$

$$\tau_f^o = F_t^o r_o^o - \tau_m^o - \dot{\omega}_2^o I_b \tag{13}$$

$$\tau_b^o = \tau_m^o - \dot{\omega}_2^o I_a \tag{14}$$

$$\tau_i^o = \dot{\omega}_2^o (I_a + I_b) \tag{15}$$

Materials and Methods

In this section, we present the necessary reference conditions and methodology for reproducing our experimental and theoretical results.

Material and Lubricant Properties

The test rollers R1 and R2 are made of high-strength chromium-molybdenum alloy steel. The top roller (R2) was nitrocarburized to enhance its hardness. The elastic modulus E_{R1} and E_{R_2}, Poisson's ratio ν_{R1} and ν_{R2}, and the hardness HV_{R1} and HV_{R2} are presented in Table 1. Both rollers were machined to attain a surface roughness $Rq \approx 0.45\,\mu\text{m}$. The surface roughness was measured by using a 3D profiler Sensofar S Neox optical microscope in confocal mode with 10x magnification.

To lubricate the contact under study, the bottom roller R1 was partially immersed in an oil bath with high-viscosity (ISO-VG 680) mineral oil. The dynamic viscosity at 40 °C ($\eta_{40\circ}$) and 100 °C ($\eta_{100\circ}$), and density (ρ_{lub}) at 20 °C were provided by the supplier (Table 1). The needle bearings were lubricated with grease, which comprised a calcium sulphonate complex thickener (CaS) and a polyalphaolefin (PAO) base oil. The kinematic viscosities of the PAO base oil at 40 °C ($\nu_{40\,^\circ\text{C}}$) and 100 °C ($\nu_{100\,^\circ\text{C}}$) were provided by the supplier (Table. 1).

The experiments were conducted at a temperature of 20 °C (room temperature) for practical considerations. The primary reason was to maintain a high viscosity and fully avoid surface damage, especially for cases where full sliding could occur, and, thus, eliminate any variations resulting from wear. For the first test, the inlet temperature T_0 was assumed to be 20 °C for both, the contact under study and the needle bearings. However, during each of the following experiments, the surface of the rollers showed a small temperature increase. These temperature changes were measured on the top roller R2 on a non-contacting section (adjacent to the contact) with high emissivity. For that, an infrared thermometer gun was used. The effects of these temperature changes will be further explained in the section "Results and Discussion". To compute the viscosities (η_0 and ν) at 20 °C and other temperatures, the ASTM standard[25] was followed.

The limiting shear stress coefficient Λ_{min} for the mineral oil was determined through measurements from a Mini Traction Machine (MTM). The pressure viscosity coefficient

α, the viscosity-temperature coefficient β, and the viscosity-pressure index Z were estimated by using the equations specified in reference[26]. Note that Table 1 also contains the specific heat C_{pR1} and C_{pR2}, the thermal conductivity k_{R1} and k_{R2}, and the density of steel ρ_{R1} and ρ_{R2}. These properties are required to estimate the temperature rise during the evaluation of the traction coefficient μ^o, as described in reference[22].

Table 1. Material and lubricant properties.

Parameter	Value	Unit
E_{R1}, E_{R2}	210	GPa
ν_{R1}, ν_{R2}	0.33	–
k_{R1}	46	$\mathrm{W\,m^{-1}\,K^{-1}}$
k_{R2}	21	$\mathrm{W\,m^{-1}\,K^{-1}}$
$C_{pR2}, C_{P_{R2}}$	450	$\mathrm{J\,kg^{-1}\,K^{-1}}$
ρ_{R1}, ρ_{R2}	7800	$\mathrm{kg\,m^{-3}}$
HV_{R1}	2.17	GPa
HV_{R2}	6.36	GPa
Rq_{R1}	0.45	µm
Rq_{R2}	0.45	µm
T_0	20	°C
$\nu_{40\,^\circ\mathrm{C}}$	100	$\mathrm{mm^2\,s^{-1}}$
$\nu_{100\,^\circ\mathrm{C}}$	13.4	$\mathrm{mm^2\,s^{-1}}$
ν	293.8	$\mathrm{mm^2\,s^{-1}}$
ρ_{lub}	900	$\mathrm{kg\,m^{-3}}$
$\eta_{40\,^\circ\mathrm{C}}$	0.625	Pa s
$\eta_{100\,^\circ\mathrm{C}}$	0.039	Pa s
η_0	3.04	Pa s
α	28.8	$\mathrm{GPa^-1}$
β	0.048	–
Λ_{min}	0.076	–

Table 2 provides an overview of the material, geometrical, and other relevant properties of both the input and output systems for comparison. Note that the description "Cam" and "Roller" for the input system should be interpreted as bottom and top roller, respectively, for the output system. Also, note that the cam radius corresponds to the base circle of the camring. For parameters that fluctuate from a minimum to a maximum (e.g., R', F_c, P_{max}) the ranges have been provided.

Table 2. Properties of the input (HD) and output (Test setup) systems.

Parameter	Input (HD)	Output (Test setup)
B	150 mm	11 mm
R'	$99 - 229$mm	13.5 mm
HV Cam	4.15 GPa	2.17 GPa
HV Roller	6.8 GPa	6.36 GPa
F_c	$28.3 - 449.2$kN	$0.2 - 4$kN
P_{max}	$0.2 - 1$GPa	$0.2 - 1$GPa
Cam radius	1910 mm	27 mm
Roller radius	300 mm	27 mm
Roller Inertia	$0.90\,\mathrm{kg\,m^2}$	$1.8 \times 10^{-3}\,\mathrm{kg\,m^2}$
Cam material	$Cr - Mo\ HSS$	$Cr - Mo\ HSS$
Roller material	$Cr - Mo\ HSS$	$Cr - Mo\ HSS$
Cam Rq	0.8 µm	0.4 µm
Roller Rq	0.8 µm	0.4 µm

Integration of Additional Inertia

As explained earlier, the inertia of the roller in the output system I_r^o should be substantially increased in relation to its original value ($1.47 \times 10^{-4}\,\mathrm{kg\,m^2}$). This adjustment is required when following the approach presented earlier to intensify the effects of inertia at a small scale. In that way, the rolling-sliding dynamics observed at large scales (Figure 3) could be replicated. To estimate the additional inertia required in the output system, the approach presented above can be employed as shown next.

The contact force F_c^i and maximum contact pressure P_{max}^i generated during the peak acceleration $\dot{\omega}^i = 100.7\,\mathrm{rad\,s^{-2}}$ in the input system are 440 kN and 0.77 GPa, respectively (Figure 3). The contact force F_c^o that generates a maximum contact pressure of 0.77 GPa in the output system is 2.35 kN. By making use of eq.7, with $S_1 = 5.55$, the scaling factor $S_5 = 1040$, and the scaled output roller inertia $I_r^o = 8.65 \times 10^{-4}\,\mathrm{kg\,m^2}$ can be calculated. Note that this new value is roughly 6 times above the initial inertia.

In line with our approach, the total inertia in the output system I_r^o should match $8.65 \times 10^{-4}\,\mathrm{kg\,m^2}$. However, in practice, this turned out challenging, as the inertia of the inbuilt flywheel in the brake exceeded our requirements. When falling short in inertia, an extra flywheel could be easily integrated, but, in our case, some inertia had to be removed. Given that the modifications needed to match the required inertia implied an irreversible change of the brake, we decided to keep this extra inertia in the output system. As a result, the total inertia I_r^o added up to $1.8 \times 10^{-3}\,\mathrm{kg\,m^2}$, exceeding the required value by roughly 2 times. Keeping this in consideration, one of the advantages is that the effects of inertia become more clear. And evidently, for the simulations, this extra inertia was also taken into account. More details on this matter will be given later on in section "Results and Discussion". With $I_r^o = 1.8 \times 10^{-3}\,\mathrm{kg\,m^2}$, the inertia before ($I_b$) and after ($I_a$) the torque sensor are $3.94 \times 10^{-3}\,\mathrm{kg\,m^2}$ and $1.36 \times 10^{-3}\,\mathrm{kg\,m^2}$, respectively. In terms of percentage, a 77.5 % of the total inertia is allocated to I_a and a 22.5 % to I_b.

Cyclic Loading Tests

The experiments under cyclic loading conditions were conducted in an attempt to replicate the rolling-sliding dynamics of cam-roller contacts in the large-scale HD (Figure 3). To generate a contact force profile similar to that in the input system (Figure 3), a switching signal with a frequency of 0.5 Hz was used to command a pressure regulator valve and control the pressure inside the air bellow. In that way, relatively rapid contact force changes ranging from approximately 0.2 to 4 kN were attained. This loading range, generates the required minimum (0.2 GPa) and maximum (1 GPa) P_{max}^o that matches the P_{max}^i range in the input system (Figure 3). It is important to note that the cyclic load frequency (i.e., 0.5 Hz) in the output system fell short when compared to that of the input system (i.e., 2.5 Hz). As expected, this adjustment was required due to limitations in the actuation speed. The consequences of slower contact force transitions will be discussed in section "Results and Discussion".

For all the experiments, the rotational speed of the bottom roller (R1) was maintained stable at $450\,\mathrm{rpm}$ (i.e., $\omega_1 = 47.12\,\mathrm{rad\,s^{-1}}$). By doing so, full film lubrication was ensured during the experiments.

Under low contact forces, rolling contacts exhibit increased sensitivity to an applied resisting torque, as documented in previous studies[5,20,21]. This means that, in such conditions, even a slight increase in the applied torque can result in a sharp increase in the SRR. To emphasize this aspect and generate diverse scenarios, 4 different braking torques τ_b, (0.06, 0.14, 0.22, and $0.27\,\mathrm{N\,m}$), were applied in four tests, respectively. Table 3 provides an overview of the reference conditions for all the experiments conducted under cyclic loading conditions.

Table 3. Reference conditions for the experiments.

Test	F_c [kN]	Speed (R1) [rpm]	τ_b [N m]
a	0.2 - 4	450	0.06
b	0.2 - 4	450	0.14
c	0.2 - 4	450	0.22
d	0.2 - 4	450	0.27

The duration of each loading cycle, comprising a high contact force phase and a low contact force phase, is $2\,\mathrm{s}$. Thus, to complete 300 loading cycles, the duration of each test was configured to be $10\,\mathrm{min}$. For each test, the data was collected at a sampling rate of $500\,\mathrm{Hz}$. The measurement data from each test (comprising 300 cycles), was processed to compute the average cycle for various parameters including contact force F_c^o, maximum contact pressure P_{max}^o, slide-to-roll ratio SRR^o, and traction force F_t^o, respectively. This approach substantially improved the significance of the results and generated exceptionally smooth plots. Consequently, there was no need for additional data filtering or smoothing procedures, other than the averaging of the different cycle measurements into one overall cycle.

Results and Discussion

In this section, a series of plots containing the results of the experiments and predictions will be presented. Note that the superscript "*" has been used for the predicted results. All the plots in figures 6, 7 and 8, show the cycle time in the x-axis. As explained earlier, the profiles in the graphs correspond to average cycles calculated from 300 cycles, respectively.

In Figure 6, the plots on the left show the SRR^o and contact force F_c profiles. The central lines (at time $1\,\mathrm{s}$) divide the high contact force phase from the low contact force phase. The plots on the right show the traction force F_t^o and maximum Hertzian contact pressure P_{max}^o profiles. In Figure 7, the plots on the left show the smearing criterion ϕ and contact force F_c profiles. The plots on the right show the angular acceleration $\dot{\omega}^o$ and maximum Hertzian contact pressure P_{max}^o profiles. In Figure 8, the plots on the left show the Hertzian contact area A^o and maximum Hertzian contact pressure P_{max}^o profiles. The plots on the right show the shear stress τ_o and contact force F_c^o profiles. Finally, Figure 9 shows the bottom roller R1 before and after the experiments.

Table 4 contains the inlet temperature T_0 and lambda ratios λ for tests a, b, c, and d, respectively. Note that in spite of the temperature changes, the lambda ratios λ indicate that all the experiments were conducted under full film lubrication. Hence, as expected, wear did not occur (Figure 9).

Table 4. Inlet temperatures T_0 and lambda ratios λ.

Test	T_0 [°C]	Min. λ [−]	Max. λ [−]	Avg. λ [−]
a	20	13.5	16.6	14.6
b	22	11.7	14.1	12.6
c	25	9.6	11.3	10.2
d	29	6.9	8.7	7.8

For the sake of clarity, this section is divided into three parts. In the first part, we will judge how well the rolling-sliding dynamics of the large-scale input system can be replicated in the simplified small-scale output system. In the second part, we will assess the impact of the resisting torque on the rolling-sliding dynamics. In the final part, we will evaluate the validity of the modeling framework implemented in this study by comparing the experimental and predicted results.

Replication of Rolling-Sliding Dynamics

Similarities and Differences. To begin with, it is essential to describe how well our approach enables us to reproduce the five key characteristics observed at large scales (Figure 3a and 3b). For that, we will use the results shown in Figure 6b as an example. The slide-to-roll ratio SRR^o profile in Figure 6b, exhibits the four following characteristics: (1) the roller slips at low contact forces, (2) the roller enters the high contact force phase with a certain level of slippage, (3) the roller transitions rapidly from rolling-sliding to virtually pure rolling, (4) the roller rolls without slipping under high contact forces, and then, the cycle repeats. A fifth characteristic (5), i.e., the large peak in the traction force F_t^o profile, is also visible in Figure 6b. Similar to that at a large scale, this traction force peak occurs as a result of the rapid change in the rolling conditions. Likewise, the latter is also responsible for the peak in the roller's angular acceleration $\dot{\omega}^o$ shown in Figure 7b.

While our approach can in essence replicate the rolling-sliding dynamics observed at large scales, it is crucial to emphasize the differences as well. Perhaps one of the most important differences regards the contact force F_c^o profile (Figure 6). In the output system, the loading cycle is 5 times slower, and the transitions from low-to-high and high-to-low contact force take roughly 12 times longer than that in the input system (Figure 3). The implications of slower contact force transitions will be discussed later on. Another difference regards the maximum Hertzian contact pressure P_{max}^o and Hertzian contact area A^o profiles (Figure 8). Since with a two-roller configuration, there are no changes in curvature, the two latter profiles match perfectly and they follow the shape of the contact force F_c^o profile. This does not apply to the input system (Figure 3). There are a few other differences that arise as a result of representing the cam-roller pair with a two-roller contact. In the input system, the kinematics of the cam-roller pair involve accelerations and decelerations that are responsible for the nuances observed

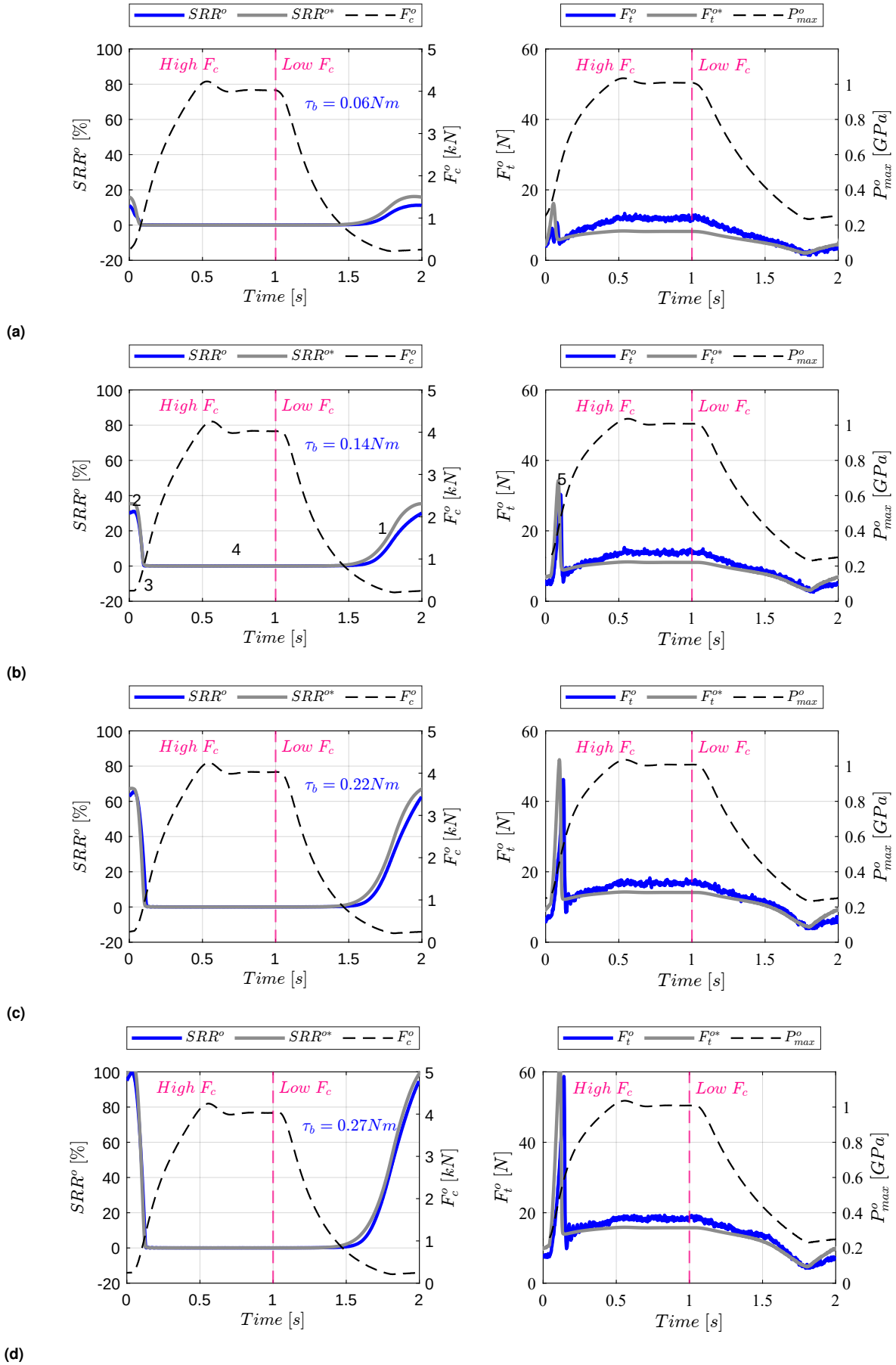

Figure 6. Measured and predicted slide-to roll ratio SRR and traction force F_t profiles. (a) $\tau_b = 0.06\,\mathrm{N\,m}$. (b) $\tau_b = 0.14\,\mathrm{N\,m}$. (c) $\tau_b = 0.22\,\mathrm{N\,m}$. (d) $\tau_b = 0.27\,\mathrm{N\,m}$.

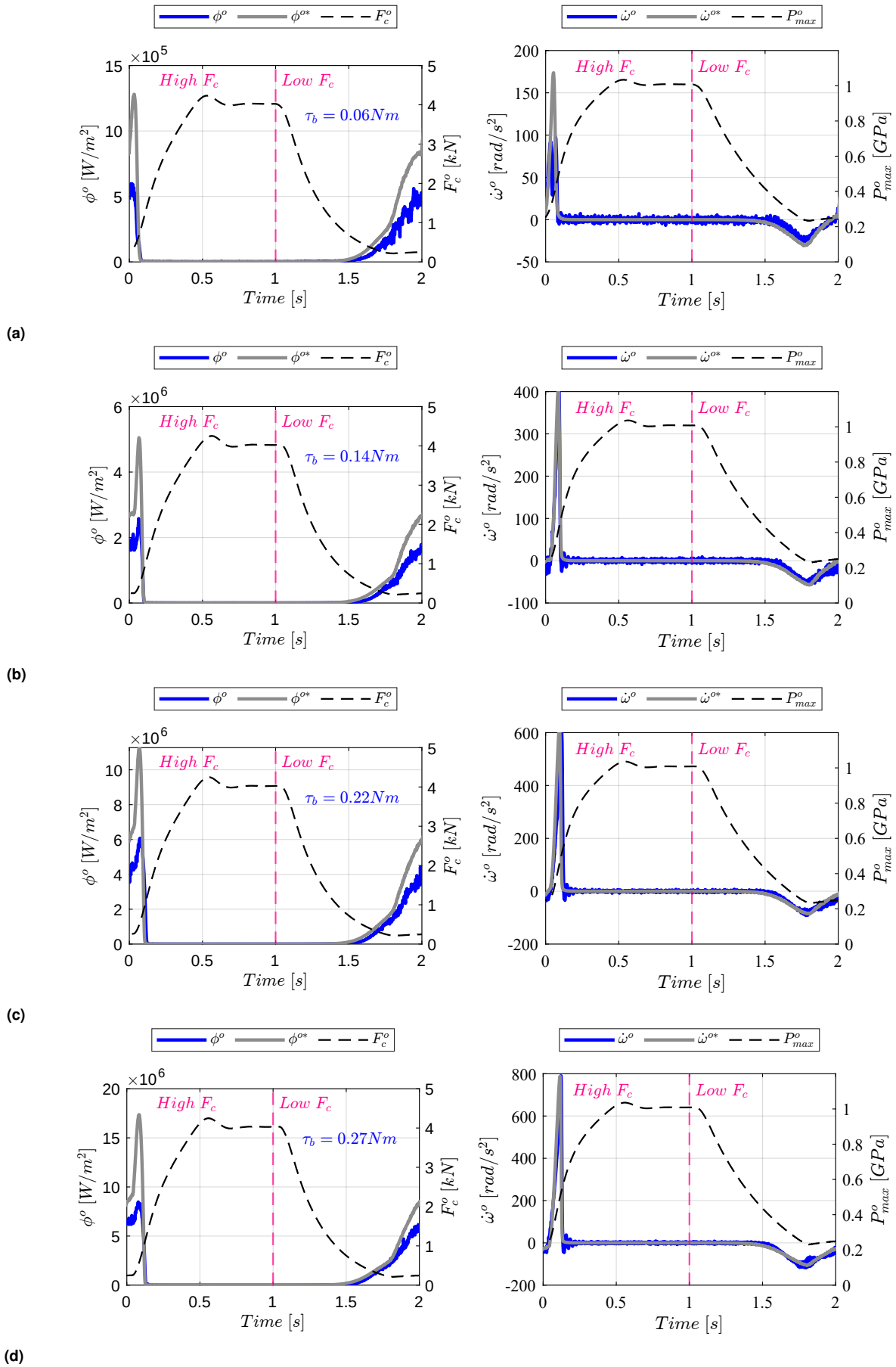

Figure 7. Measured and predicted smearing criterion ϕ and angular acceleration $\dot{\omega}_2$. (a) $\tau_b = 0.06\,\mathrm{N\,m}$. (b) $\tau_b = 0.14\,\mathrm{N\,m}$. (c) $\tau_b = 0.22\,\mathrm{N\,m}$. (d) $\tau_b = 0.27\,\mathrm{N\,m}$.

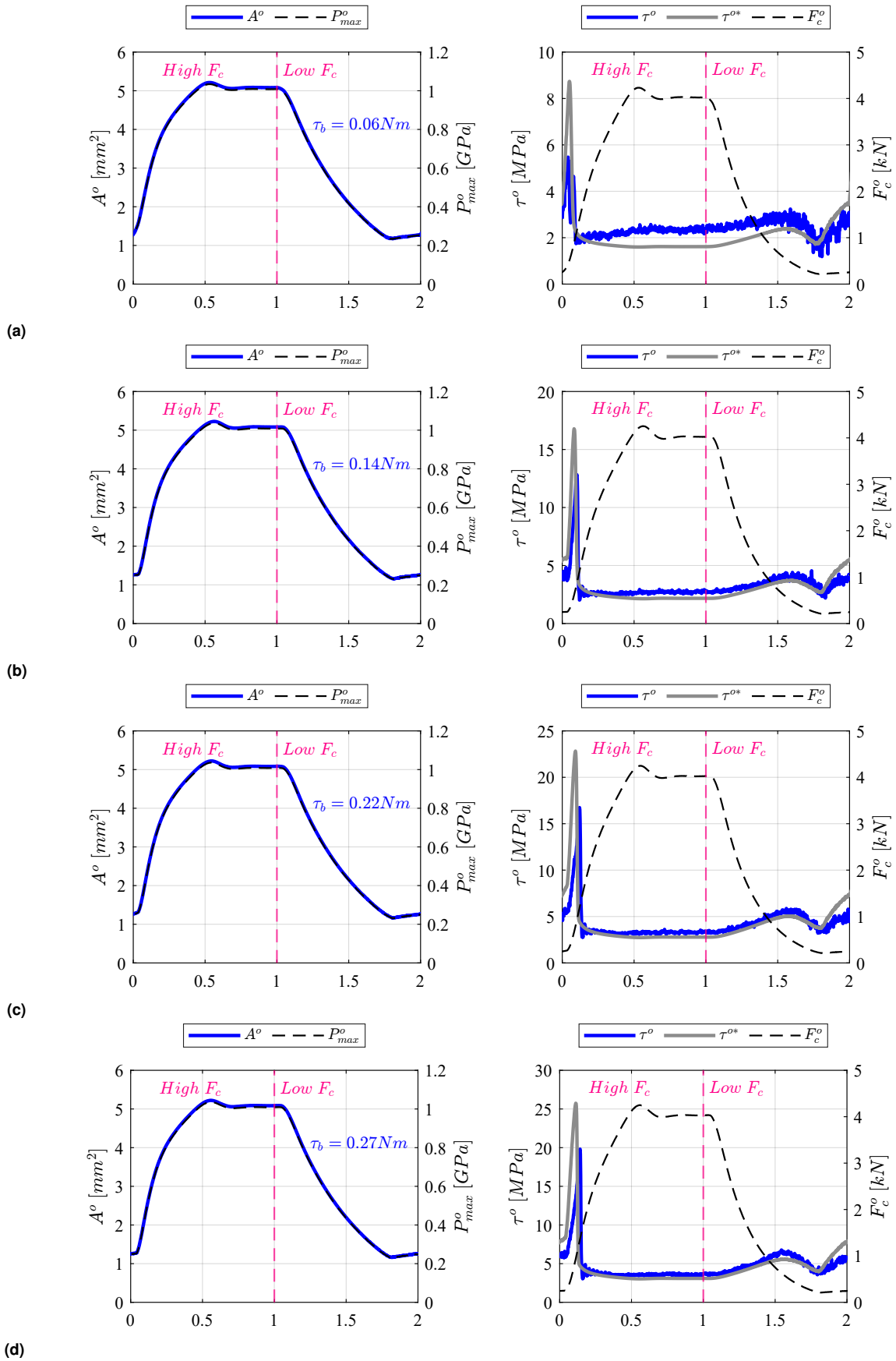

Figure 8. Calculated Hertzian contact area A^o, measured shear stress τ^o, and predicted shear stress τ^{o*}.(a) $\tau_b = 0.06\,\mathrm{N\,m}$. (b) $\tau_b = 0.14\,\mathrm{N\,m}$. (c) $\tau_b = 0.22\,\mathrm{N\,m}$. (d) $\tau_b = 0.27\,\mathrm{N\,m}$.

when comparing the rolling-sliding dynamics of the input and output systems.

For example, in the output system, the slide-to-roll ratio SRR^o does not decrease when approaching the end of the

Table 5. Maximum slide-to-roll ratio SRR^o, traction force F_t^o, smearing criterion ϕ^o, angular acceleration $\dot{\omega}^o$, and shear stress τ^o measured in the output system during the tests.

Test	Max. SRR^o $[-]$	Max. F_t^o [N]	Max. ϕ^o $[\mathrm{W\,m^{-2}}]$	Max. $\dot{\omega}^o$ $[\mathrm{rad\,s^{-2}}]$	Max. τ^o [MPa]
a	11.3	10.7	5.97×10^5	97.3	5.5
b	31.1	30.3	2.58×10^6	402.9	12.8
c	65.4	46.2	6.07×10^6	598.3	16.7
d	99.6	58.7	8.47×10^6	789.7	19.8

Table 6. Maximum slide-to-roll ratio SRR^{o*}, traction force F_t^{o*}, smearing criterion ϕ^{o*}, angular acceleration $\dot{\omega}^{o*}$, and shear stress τ^{o*} predicted by the model for the output system.

Test	Max. SRR^{o*} $[-]$	Max. F_t^{o*} [N]	Max. ϕ^{o*} $[\mathrm{W\,m^{-2}}]$	Max. $\dot{\omega}^{o*}$ $[\mathrm{rad\,s^{-2}}]$	Max. τ^{o*} [MPa]
a	16.2	16.2	1.28×10^6	173.7	8.7
b	35.4	34.2	5.05×10^6	405.5	16.8
c	67.4	51.8	1.13×10^7	624.4	22.8
d	103.6	64.3	1.74×10^7	787.4	25.7

cycle (Figure 6). The effects of this are reflected in the smearing criterion ϕ^o profile (Figure 7). Another example is that the acceleration $\dot{\omega}^o$ profile in the output system is only a result of the occurrence of slippage (Figure 7). On the other hand, the accelerations in the input system occur due to roller slippage too, but also due to the kinematics of the cam-roller pair (Figure 3c). This explains why in the output system, the traction force F_t^o profile exhibits only a drop when slippage occurs and a peak when slippage quickly vanishes.

Matching the Input System. The plots a, b, c, and d, in Figures 6, 7, and 8 correspond to the braking torques τ_b^o, 0.06, 0.14, 0.22 and $0.27\,\mathrm{N\,m}$, respectively. When it comes to replicating the conditions observed in the input system, the results of test a are the closest match. It should be noted that a braking torque τ_b^o of $0.06\,\mathrm{N\,m}$ is extremely small. It is the lowest amount of resistance that can be generated with the magnetic hysteresis brake. This corresponds to a residual resisting torque that cannot be removed. In test a, the residual braking torque τ_b^o plus the small frictional torque τ_f^o generated by the needle bearings was enough to produce a maximum SRR^o of $11.3\,\%$ during the low contact force phase (Figure 6a). This SRR is in line with $SRR^i = 11.4\,\%$, which corresponds to the maximum SRR generated in the input system (Figure 3a). Concerning the traction force F_t^o, a peak was generated, but it did not correspond to a maximum (Figure 6a). Particularly in this case, the component of the traction force F_t^o generated by the frictional torque τ_f^o at high contact forces F_c^o, emerged as the dominant factor.

At this point, verifying the assumptions made when presenting the approach for scaling inertia is important. By looking at Figure 7a, it can be seen that a peak acceleration $\dot{\omega}^o = 97.3\,\mathrm{rad\,s^{-2}}$ was generated in the output system. This acceleration is very close to $100.7\,\mathrm{rad\,s^{-2}}$, which is the peak acceleration $\dot{\omega}^i$ in the input system (Figure 3c). Therefore, the first assumption remains valid. However, the peak acceleration $\dot{\omega}^o$, does not occur at a maximum Hertzian contact pressure P_{max}^o of $0.77\,\mathrm{GPa}$, but at $P_{max}^o = 0.46\,\mathrm{GPa}$ (Figure 7a). Hence, the second assumption is less valid. Consequently, the maximum shear stress generated in the output system (i.e., $\tau^o = 5.5\,\mathrm{MPa}$) is larger than that in the input system (i.e., $\tau^i = 1.36\,\mathrm{MPa}$), since at lower contact pressures, the peak traction force F_t^o acts over a smaller contact area A^o. This difference can be attributed in part to the slow contact force transitions and in another part to excessive added inertia I_r^o, as described in the following section.

It is important to mention that our study primarily aims to provide a method to scale inertia and an experimental technique to replicate the rolling-sliding dynamics of a large-scale system in a smaller-scale test setup. As such, our approach did not involve generating identical contact conditions in terms of lubrication regimes for both systems. Instead, we deliberately generated higher lambda ratios in the small-scale system to ensure the total elimination of wear. Additionally, it is important to mention that size can influence the thermal effects in EHL contacts, reducing traction at large-scales. The interested reader is referred to references[27,28] where size effects are comprehensively studied.

Effects of Exceeding the Required Inertia. As mentioned earlier, due to practical reasons, the experiments were conducted with roughly 2 times the inertia I_r^o resulting from the proposed scaling approach. On the positive side, the effects of inertia were amplified, and hence, much more visible. However, in test a, the traction force F_t^o peak, the maximum shear stress τ^o, and the maximum smearing criterion ϕ^o exceed that of the input system. This precisely suggests that a better match with the input conditions can be attained by incorporating the inertia resulting from the proposed scaling approach (i.e., $I_r^o = 8.65 \times 10^{-4}\,\mathrm{kg\,m^{-2}}$). In addition, another aspect required to achieve a better match is a substantially faster contact force transition. The latter could be for example achieved with heavy-duty linear solenoids, which we have already acquired for future work.

The Impact of Higher Resisting Torques

The influence of small increments in the resisting torque can be readily seen in Figure 6. Higher braking torques τ_b, cause a substantial increase in the SRR, but only under low contact forces. Under such conditions, the interface becomes tremendously sensitive to the applied resisting torque. At large SRRs, the traction force peaks gain intensity, and in turn, this increases the magnitude of the peak smearing criterion (Figure 7), and the peak shear stress (Figure 8).

To give an example, taking the input system into consideration (i.e., the cam-roller system in the HD), an increase in the resisting torque can occur during lubrication

and re-lubrication of the bearings. When conducting this tasks, the frictional torque generated by the bearings can increase to about to four times the originally calculated value[29]. As a consequence of this rise in the resisting torque, the SRR at the cam-roller contact generated under low contact forces could substantially increase, leading to the emergence of high-intensity peaks in the traction force. Consequently, the surface temperature of the roller would increase, the film thickness would drop, and smearing damage would be more likely to occur.

It is important to highlight that the occurrence of slippage under low contact forces and full film lubrication might not be harmful. However, what poses a concern is the brusque change in the rolling conditions arising at the beginning of the high contact force phase. Another important aspect regards thermal effects. As previously explained, a rise in surface temperature occurs at large SRRs. Subsequently, this can lead to a reduction in the minimum film thickness, potentially resulting in mixed or boundary lubrication, and thus, wear. Therefore, minimizing roller slippage remains an essential aspect. Table 5 summarizes the maximum value of different parameters measured during the experiments at different resisting torques.

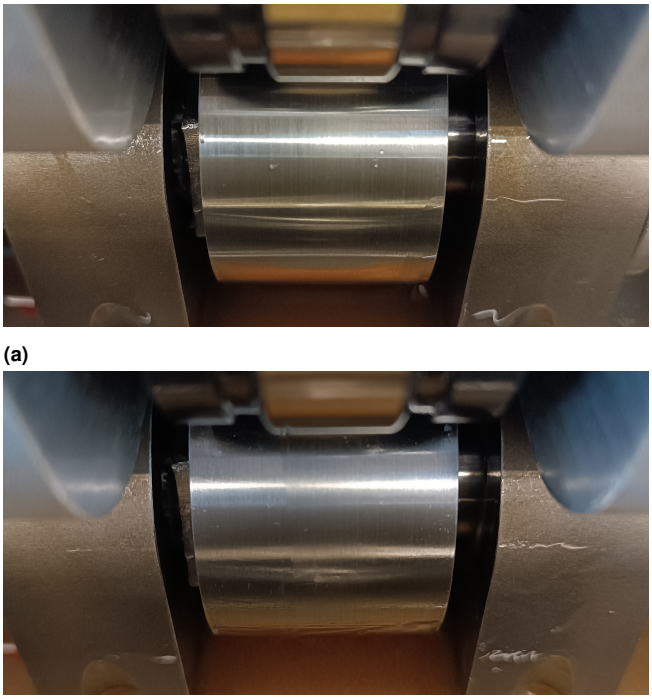

(a)

(b)

Figure 9. Bottom test roller (R1). (a) Before the experiments. (b) After the experiments.

Model Validation and Comparison

As previously mentioned, a temperature rise on the surface of the rollers was observed during the experiments, particularly at large SRRs (Table 4). For that reason, an increase in the inlet temperatures T_0 was also accounted for in the model to adjust the dynamic viscosity η_0, the limiting shear stress coefficient Λ, and the pressure-viscosity coefficient α values. Temperature changes were considered only in the lubrication model used for predicting the traction coefficient μ^o. In contrast, for estimating the frictional torque τ_f, a constant temperature of 22 °C was assumed. This decision was rooted in the fact that temperature changes in the needle bearings were less significant and viscosity changes in eq.11, have virtually no influence on the frictional torque. Table 7 contains the respective updates on the lubricant properties.

Table 7. Adjusted lubricant properties.

Test	T_0 [°C]	η_0 [Pa s]	Λ [−]	α [GPa^{-1}]
a	20	3.04	0.076	28.8
b	22	2.54	0.075	28.4
c	25	1.96	0.073	27.7
d	29	1.41	0.071	26.8

As shown in Figure 6, 7, and 8, the model effectively captures prominent trends and produces reasonable results. It demonstrates its capability to predict the magnitude, shape, and position of relevant features in key parameters, including the slide-to-roll ratio SRR^{o*}, the traction force F_t^{o*}, smearing criterion ϕ^{o*}, angular acceleration $\dot{\omega}^{o*}$, and shear stress τ^{o*}. Hence, we have confidence that the predictions generated by the framework utilized in this study offer valuable insights into the rolling-sliding dynamics in line contacts operating under cyclic loads and full film lubrication. The values in Table 6 correspond to the maximum predicted values for the parameters mentioned above. These values can be compared to those in Table 5.

It is also important to address the disparities observed in the results. One of them is the difference between the predicted (F_t^{o*}) and the measured (F_t^o) traction force, particularly at high contact forces. This discrepancy can be seen in the traction force F_t^o plots in Figure 6 during the high F_c phase, particularly from 0.5 to 1 s. In all cases, the measured traction force exceeded the predicted value by approximately 1.5 to 3 N. It should be noted that from time 0.2 to 1.4 s, there are no changes in speed (i.e., SRR=0), and thus, the inertia torque τ_i^o is zero. Moreover, the applied braking torque τ_b^o is an input parameter in the model. Therefore, the discrepancies in the predicted traction force (F_t^{o*}) observed in this region can be attributed to an underestimation of the frictional torque τ_f^o, which is then reflected in the predicted traction force F_t^{o*} as a result of torque balancing (eq.9). We suspect that the frictional torque in our test setup (computed with eq.13) slightly exceeds the estimated frictional torque (computed with eq.11) due to the non-self-aligning nature of the needle-bearing arrangement. This implies that, under heavy loads, the bearings do not compensate for shaft bending, resulting in some additional resistance.

It is also worthwhile noting that the position of the predicted traction force F_t^{o*} peak, is somewhat shifted to the left. The reason for this is a slight overestimation of the traction coefficient μ^{o*}. In part, this variation may be attributed to the uncertainty in the estimated rheological properties of the lubricant.

The effects of overestimating the traction coefficient μ^{o*} are also reflected on the predicted smearing criterion ϕ^{o*} (Figure 7). As for predictions of the angular acceleration $\dot{\omega}^{o*}$, two scenarios become apparent: when the maximum SRR^{o*} is overestimated (e.g., 6a), an overestimation of the

angular acceleration is also observed. Conversely, when the maximum SRR^{o*} is underestimated (e.g., 6b, 6c, 6d), the angular acceleration is likewise underestimated. Finally, the overestimation and position shift in the predicted shear stress τ^{o*} can also be linked to the shift of the traction force peak mentioned earlier.

Conclusions

In this work, we have presented an approach to replicate the rolling-sliding dynamics of cam-roller contacts in a large-scale hydraulic drivetrain (i.e., the input system) on a small-scale two-roller test setup (i.e., the output system). To downscale inertia effectively, we proposed a method based on equating the shear stress during peak accelerations in both systems. Besides, we have implemented a theoretical framework from previous work, to predict the rolling-sliding dynamics of the output system under various conditions.

The proposed approach effectively reproduces the five key characteristics observed in the input system, including the effects of rapid changes in rolling conditions. The results on a small scale showed significant similarities to those anticipated at a large scale, but slow contact force transitions in the output system contributed to differences. This was considered an important point for improvement in future work.

Regarding the applied resisting torque, its impact on the rolling-sliding dynamics was evident, particularly during the low contact force phase. Small increments in the braking torque led to very large SRRs. Consequently, the peak traction force, shear stress, and smearing criterion were intensified. At a large scale, an increase in the resisting torque can be anticipated during the re-lubrication of the internal spherical roller bearings. In turn, this may lead to high SRRs. Such a scenario presents a concern when considering the brusque transition in rolling conditions experienced at the start of the high contact force phase. Therefore, finding solutions to mitigate slippage is another important point for future work.

Finally, the modeling framework employed in this work provided reasonable predictions. Overall, good agreement with the experimental results was observed. The model effectively captured prominent trends and provided results with reasonable accuracy for various parameters. From an engineering perspective, this modeling framework can provide valuable insight into the rolling-sliding dynamics of rolling contacts subjected to cyclic loads. Nevertheless, the existence of disparities was also addressed. Differences in the predicted and measured traction force profiles were primarily attributed to an underestimation of frictional torque, possibly due to the non-self-aligning nature of the needle-bearing arrangement in the test setup. Additionally, a slight overestimation of the traction coefficient was observed. This was partly attributed to uncertainties in the estimated rheological properties of the lubricant. In addition to that, discrepancies in the predictions for the angular acceleration were observed as a result of the accuracy of the slide-to-roll ratio estimation. These limitations highlight the possibilities for refinement in the model and a closer examination of experimental conditions for further improvement.

Acknowledgements

The research presented in this paper is part of the DOT3000 project and was conducted by Delft University of Technology in collaboration with Delft Offshore Turbine (DOT).

Declaration of Conflicting Interests

The author(s) declared no potential conflicts of interest with respect to the research, authorship, and/or publication of this article.

Funding

The authors disclosed receipt of the following financial support for the research, authorship, and/or publication of this article: The research presented in this paper is part of the DOT3000 project, which was conducted by Delft University of Technology in collaboration with Delft Offshore Turbine (DOT) and executed with funding received from the Dutch ministry of economic affairs via TKI Wind at Sea, Top sector Energy, project number [TEHE119007].

References

1. Chen W, Wang X, Zhang F, Liu H, Lin Y. Review of the application of hydraulic technology in wind turbine. Wind Energy. 2020;23(7):1495-522.
2. Diepeveen N. On fluid power transmission in offshore wind turbines [PhD thesis]. Delft University of Technology; 2013.
3. Paul Mulders S, Frederik Boudewijn Diepeveen N, Van Wingerden JW. Control design, implementation, and evaluation for an in-field 500 kW wind turbine with a fixed-displacement hydraulic drivetrain. Wind Energy Science. 2018;3(2):615-38.
4. Nijssen J, Kempenaar A, Diepeveen N. Development of an interface between a plunger and an eccentric running track for a low-speed seawater pump. In: Proceedings 11th International Fluid Power Conference. vol. 1. Power Networks Citation; 2018. p. 370-9.
5. Amoroso P, van Ostayen RAJ, Perassi F. Rolling-Sliding Performance of Radial and Offset Roller Followers in Hydraulic Drivetrains for Large Scale Applications : A Comparative Study. MDPI Machines. 2023;11(6):604.
6. Gecim BA. Lubrication and fatigue analysis of a cam and roller follower. Tribology Series. 1989;14.
7. Duffy PE. An Experimental Investigation of Sliding at Cam to Roller Tappet Contacts. SAE Technical Paper 930691. 1993.
8. Lee J, Patterson DJ. Analysis of Cam/Roller Follower Friction and Slippage in Valve Train Systems. SAE Technical Paper 951039. 1995.
9. Lee J, Patterson DJ, Morrison KM, Schwartz GB. Friction Measurement in the Valve Train with a Roller Follower. SAE Technical Paper 940589. 1994.
10. Ji F, Taylor CM. A tribological study of roller follower valve trains. Part 1: A theoretical study with a numerical lubrication model considering possible sliding. Tribology Series. 1998;34:489-99.
11. Alakhramsing SS, de Rooij M, Schipper DJ, van Drogen M. Lubrication and frictional analysis of cam–roller follower mechanisms. Proceedings of the Institution of Mechanical

Engineers, Part J: Journal of Engineering Tribology. 2018 3;232(3):347-63.
12. Alakhramsing SS, de Rooij MB, Schipper DJ, van Drogen M. A full numerical solution to the coupled cam–roller and roller–pin contact in heavily loaded cam–roller follower mechanisms. Proceedings of the Institution of Mechanical Engineers, Part J: Journal of Engineering Tribology. 2018 10;232(10):1273-84.
13. Hamer C. Smearing in Rolling Element Bearings [PhD thesis]. University of London; 1991.
14. Evans RD, Barr TA, Houpert L, Boyd SV. Prevention of Smearing Damage in Cylindrical Roller Bearings. Tribology Transactions. 2013;56(5):703-16.
15. Hamer JC. An Experimental Investigation Into the Boundaries of Smearing Failure in Roller Bearings. Journal of Tribology. 1991;113(1):102-19.
16. Colechin M, Stone CR, Leonard HJ. Analysis of Roller-Follower Valve Gear. SAE Technical Paper 930692. 1993;n/a(5).
17. Khurram M, Mufti RA, Zahid R, Afzal N, Bhutta MU, Khan M. Effect of lubricant chemistry on the performance of end pivoted roller follower valve train. Tribology International. 2016 1;93:717-22.
18. Abdullah MU, Shah SR, Bhutta MU, Mufti RA, Khurram M, Najeeb MH, et al. Benefits of wonder process craft on engine valve train performance. Proceedings of the Institution of Mechanical Engineers, Part D: Journal of Automobile Engineering. 2019 4;233(5):1125-35.
19. Chiu YP, Myers M. A rational approach for determining permissible speed for needle roller bearings. SAE Technical Papers. 1998;107:330-7.
20. Alakhramsing SS, de Rooij MB, Akchurin A, Schipper DJ, van Drogen M. A mixed-TEHL analysis of cam-roller contacts considering roller slip: On the influence of roller-pin contact friction. Journal of Tribology. 2019 1;141(1).
21. Amoroso P, Vrček A, de Rooij M. A Novel Tribometer and a Comprehensive Testing Method for Rolling-Sliding Conditions. MDPI Machines. 2023;11(11):1-19.
22. Masjedi M, Khonsari MM. An engineering approach for rapid evaluation of traction coefficient and wear in mixed EHL. Tribology International. 2015 7;92:184-90.
23. Moes H. Lubrication and beyond. Enschede: University of Twente; 2000. Available from: http://scholar.google.com/scholar?hl=en&btnG=Search&q=intitle:Lubrication+and+beyond#0%0Ahttps://www.utwente.nl/ctw/tr/Organisation/Links/Moes.pdf.
24. Marian M, Bartz M, Wartzack S, Rosenkranz A. Non-dimensional groups, film thickness equations and correction factors for elastohydrodynamic lubrication: A review. Lubricants. 2020;8(10):1-20.
25. ASTM International. Standard Test Method for Viscosity-Temperature Charts for Liquid Petroleum Products. ASTM; 2004.
26. Khonsari MM, Booser ER. Applied Tribology: Bearing Design and Lubrication, 3rd Edition. 3rd ed. 2017 John Wiley & Sons Ltd; 2017.
27. Liu X, Cui J, Yang P. Size effect on the behavior of thermal elastohydrodynamic lubrication of roller pairs. Journal of Tribology. 2012;134(1).
28. Liu HC, Zhang BB, Bader N, Venner CH, Poll G. Scale and contact geometry effects on friction in thermal EHL: twin-disc versus ball-on-disc. Tribology International. 2021;154(September 2020):106694. Available from: https://doi.org/10.1016/j.triboint.2020.106694.
29. SKF Group. The SKF model for calculating the frictional moment; 2018. [Cited 2023 Oct 30]. Available from: https://cdn.skfmediahub.skf.com/api/public/0901d1968065e9e7/pdf_preview_medium/0901d1968065e9e7_pdf_preview_medium.pdf.

Appendix

Notation

A	Hertzian contact area	m^2
B	Contact length	m
b	Half Hertzian contact width	m
α	Pressure viscosity coefficient	GPa^{-1}
β	Viscosity-temperature coefficient	-
$C_{p_{R1,R2}}$	Specific heat	$\mathrm{J\,kg^{-1}\,K^{-1}}$
d_m	Mean bearing diameter	mm
$E_{R1,R2}$	Young's modulus	GPa
F_c	Contact force	N
F_t	Traction force	N
h_c	Central film thickness	$\mu\mathrm{m}$
h_{min}	Minimum film thickness	$\mu\mathrm{m}$
$HV_{R1,R2}$	Vickers hardness	GPa
I_r^i	Input roller inertia	$\mathrm{kg\,m^{-2}}$
I_r^o	Scaled output roller inertia	$\mathrm{kg\,m^{-2}}$
$k_{R1,R2}$	Thermal conductivity	$\mathrm{W\,m^{-1}\,K^{-1}}$
l_r	Roller length	m
λ	Lambda ratio	-
Λ_{min}	Limiting shear stress coefficient	-
μ	Traction coefficient	-
ν	Kinematic viscosity	$\mathrm{mm^2\,s^{-1}}$
$\nu_{R1,R2}$	Poisson's ratio	-
n	Needle bearing speed	rpm
P_{max}	Max. Hertzian contact pressure	GPa
$\rho_{R1,R2}$	Density	$\mathrm{kg\,m^{-3}}$
ρ_{lub}	Lubricant density	$\mathrm{kg\,m^{-3}}$
r_i	Roller inner radius	m
r_o	Roller outer radius	m
R'	Equivalent contact radius	m
$R1$	Bottom roller	-
$R2$	Top roller	-
$Rq_{R1,R2}$	Root mean square roughness	$\mu\mathrm{m}$
S_{1-5}	Scaling factors	-
SRR	Slide-to-roll ratio	-
σ	Roller follower displacement	m
σ^*	Composite surface roughness	m
T_0	Inlet temperature	$^\circ\mathrm{C}$
u_1^o	R1 tangential speed	$\mathrm{m\,s^{-1}}$
u_2^o	R2 tangential speed	$\mathrm{m\,s^{-1}}$
u_c	Cam surface velocity	$\mathrm{m\,s^{-1}}$
u_m	Mean entrainment velocity	$\mathrm{m\,s^{-1}}$
u_r	Roller surface velocity	$\mathrm{m\,s^{-1}}$
u_s	Sliding velocity	$\mathrm{m\,s^{-1}}$
τ	Shear stress	MPa
τ_b	Braking torque	$\mathrm{N\,m}$
τ_d	Driving torque	$\mathrm{N\,m}$
τ_f	Frictional torque	$\mathrm{N\,m}$
τ_i	Inertia torque	$\mathrm{N\,m}$
τ_m	Measured torque	$\mathrm{N\,m}$
τ_t	Tractive torque	$\mathrm{N\,m}$
τ_{lim}	Limiting shear stress	Pa
ϕ	Smearing criterion	$\mathrm{W\,m^{-2}}$
$\dot{\omega}$	Angular acceleration	$\mathrm{rad\,s^{-2}}$
$\dot{\omega_2}$	R2 angular acceleration	$\mathrm{rad\,s^{-2}}$
ω_1^o	R1 rotational speed	$\mathrm{rad\,s^{-1}}$
ω_2^o	R2 rotational speed	$\mathrm{rad\,s^{-1}}$